LAWRENCE
LIVERMORE
NATIONAL
LABORATORY

LLNL-JRNL-800568

Thermal Transport Modeling of Laser-irradiated Spheres

K. H. Ma, M. V. Patel, M. Sherlock, W. A. Farmer, E. Johnsen

January 6, 2020

Physics of Plasmas

Disclaimer

Thermal transport modeling of laser-irradiated spheres

K.H. Ma,[1, a)] M.V. Patel,[2, b)] M. Sherlock,[2] W.A. Farmer,[2] and E. Johnsen[1, c)]
[1)]*University of Michigan, Ann Arbor, MI 48108, USA*
[2)]*Lawrence Livermore National Laboratory, Livermore, California 94551, USA*

(Dated: 12 February 2020)

Thermal transport of uniformly laser-irradiated spheres of various materials is investigated computationally. One-dimensional simulations of low- to mid-Z materials (Be, Al, Cu) are performed to evaluate the role of nonlocal electron transport on experimental observables under laser intensities of relevance to direct-drive inertial confinement fusion. We compare thermal transport models of different levels of sophistication: flux-limited Spitzer-Harm diffusion, the Schurtz-Nicolai-Busquet (SNB) reduced-order nonlocal model, and a Fokker-Planck description. Spitzer-Harm diffusion with different flux-limiter factors are compared with different implementations of the SNB model in the HYDRA radiation hydrodynamics code. Under the conditions of interest, the peak heat flux from in the thermal front from the SNB model shows good agreement with Fokker-Planck calculations, with the largest errors below 20% at 10^{15} W/cm^2 laser intensity. From HYDRA-SNB simulations, two experimentally relevant effects are observed from nonlocal heat transport when compared to flux-limited Spitzer-Harm modeling: coronal temperatures are cooler due to reduced heat fluxes in the expanding corona, and (for mid-Z materials) X-ray emissions are increased from preheating in the dense plasma.

I. INTRODUCTION

Modeling of electron thermal transport plays a significant role in simulations of laser-generated plasmas related to inertial confinement fusion (ICF) experiments. However, at laser intensities relevant to direct-drive ICF ($10^{14} - 10^{15}$ W/cm^2), steep temperature gradients are generated and the electron transport departs from classical[1]. The subsequent transport exhibits nonlocal effects such as heat flux inhibition at steep gradients in electron temperature, and long-range heating of the plasma, or preheat[2].

In radiation hydrodynamic codes, thermal transport is commonly modeled by classical Spitzer-Harm local diffusion[3], in which the local heat flux $Q_{SH} = -\kappa_{SH}\nabla T_e$, where T_e is the electron temperature, and the thermal conductivity κ_{SH} is proportional to $T_e^{5/2}$. This local diffusion representation of heat flux is valid when the temperature gradient scale-length $L_T = T_e/|\nabla T_e|$ is much larger than the electron mean-free-path λ_{ei}, defined as:

$$\lambda_{ei} = \frac{T_e^2}{4\pi Z n_e e^4 \Lambda_{ei}}, \tag{1}$$

where T_e is the electron temperature, n_e and e the electron density and charge respectively, and Λ_{ei} is the Coulomb logarithm for electron-ion interactions. Generally, Spitzer-Harm transport is valid when $\lambda_{ei}/L_T > 0.01$, however ICF experiments often do not satisfy this requirement for the classical Spitzer-Harm heat flux, and the hot temperatures and steep temperature gradients result in unreasonably high local electron thermal fluxes. This issues is addressed by limiting the Spitzer-Harm heat flux to the free-stream heat flux, $Q_{FS} = n_e k_B T_e v_e$ multiplied by a flux-limiter factor f, where n_e is the electron number density and v_e is the local electron thermal velocity. Ultimately, the choice for f is ad hoc, based on attempts to match experimental observables[4,5,6]. Furthermore, the reduced heat flux results from the delocalization of the suprathermal heat-carrying electrons with velocities $4 \times v_e$ relative to the local plasma temperature, resulting in long range preheating[2] in addition to the aforementioned local heat flux inhibition. As the Spitzer-Harm heat flux is a local diffusion term, a flux-limited approach is unable to model such effects. A higher-fidelity treatment of electron thermal transport can be achieved through numerically solving the Vlasov-Fokker-Planck (VFP) equations, which consistently calculates the electron heat flux with the evolution of the electron velocity distribution function (EDF). However, kinetic approaches provide additional computational expense due to added dimensionality, and more restrictive time steps. Additionally, it is difficult to include equations of state, atomic physics modeling, and radiation transport. As a result, the kinetic approach is not presently viable for integrated ICF simulations.

However, nonlocal effects must be considered to ensure accurate modeling of ICF experiments. For example, in direct-drive ICF, nonlocal transport is necessary to accurately predict laser-energy coupling[7], shock timing[8], perturbation instability growth[9] and preheat of the fuel core[10], which affect performance characteristics such as the implosion velocity, implosion adiabat, and peak areal density[11]. Consequently, multi-physics ICF codes often implement reduced nonlocal electron thermal transport models,a subset of which utilize a convolution kernel approach[1,12]. Two notable models are the multi-dimensional, multigroup diffusion Schurtz-Nicolai-Busquet (SNB) model[13], and the Krook collision operator Colombant-Manheimer-Goncharov (CMG) model[14]. Both of these models have demonstrated links to the VFP kinetic equations. The present work focuses on SNB, which has been implemented into the CHIC[15], DRACO and LILAC[10], FCI2[13] and HYDRA[16] ICF codes. SNB has been benchmarked against VFP codes in ICF

[a)]Electronic mail: kevima@umich.edu
[b)]Electronic mail: patel15@llnl.gov
[c)]Electronic mail: ejohnsen@umich.edu

relevant plasma conditions[17,18,19], and can be extended to incorporate magnetic fields[20].

The following studies assess nonlocal electron transport effects in low- to mid-Z direct-drive spheres, but with solid cores to focus on the laser-plasma ablation front. In relation to ICF efforts, similar experiments have been performed to study high-Z materials relevant to hohlraum design[21,22], focusing on the underlying physics relating to modeling X-ray conversion efficiencies such as radiation transport, atomic physics, and laser-plasma interactions in addition to electron transport modeling. Laser-irradiated planar foil experiments have also been performed for similar purposes[23,24,25,26,27,28], however they lack the physical advantages the spherical geometry provides in minimizing self-generated magnetic fields[29], as well as diagnostic advantages in assessing laser-coupling, X-ray emissions, and plasma conditions. Given the various physics inherent in high-Z spheres, such systems still prove challenging to model. With low- to mid-Z materials some of these physics can be decoupled, as these materials exhibit fewer ionization states, reducing uncertainties from Non-Local Thermodynamic Equilibrium (NLTE) modeling[30], and also present stronger ion Landau damping, reducing one mechanism of micro-turbulence[31]. The resulting laser-irradiated sphere system is uniquely tailored to investigating nonlocal electron transport.

The primary objective of this work is to study nonlocal transport effects in low-to mid-Z irradiated spheres at laser intensities ($10^{14}-10^{15}$ W/cm^2) relevant to ICF experiments. To this end, we assess the accuracy of the SNB model for the range of materials and laser intensities in this study via comparisons with Fokker-Planck calculations from the kinetic code K2[19]. The paper is organized as follows: In section II, we briefly describe the SNB and K2 models, as well as the radiation hydrodynamics simulation set-up in HYDRA. Sections III A and III B compare SNB and kinetic heat fluxes to assess the model performance, first in stationary plasma profiles spanning the range of the simulation study, then in a temperature evolution test. Finally, section III C compares the effects of SNB and classical Spitzer-Harm transport models in full radiation hydrodynamics HYDRA simulations, as well as how these effects propagate to experimentally measurable quantities. In particular, the coronal temperatures and X-ray emissions in mid-Z materials, which evolves differently due to nonlocal effects in contrast to flux-limited Spitzer-Harm modeling.

II. MODELS AND METHODS

A. SNB transport model

The multigroup Schurtz-Nicolai-Busquet (SNB) nonlocal model[13] defines the nonlocal heat flux, $\mathbf{Q}_t$, as a sum of nonlocal corrections to the Spitzer-Harm heat flux $\mathbf{Q}_{sh}$ from N groups discretized in the electron energy distribution:

$$\mathbf{Q}_t(\mathbf{r}) = \mathbf{Q}_{sh}(\mathbf{r}) - \sum_g^N \frac{\lambda_{g,ei}(\mathbf{r})}{3}\nabla H_g(\mathbf{r}), \tag{2}$$

Here $\lambda_{g,ei}(\mathbf{r})$ is the group electron-ion mean-free-path (mfp), and $H_g(\mathbf{r})$ is calculated from multigroup steady state diffusion transport equations:

$$\left(\frac{r}{\lambda_{g,ee}(\mathbf{r})} - \nabla\cdot\frac{\xi\lambda_{g,ei}(\mathbf{r})}{3}\nabla\right)H_g(\mathbf{r}) = -\nabla\cdot\mathbf{U}_\mathbf{g}, \tag{3}$$

where:

$$\mathbf{U}_\mathbf{g} = \frac{1}{24}\int_{E_{g-1}/k_BT_e}^{E_g/k_BT_e}\beta^4 e^{-\beta}d\beta\mathbf{Q}_{sh}, \tag{4}$$

$$\lambda_{g,ei} = 2(E_{g-1/2}/k_BT_e)^2\lambda_{ei}, \tag{5}$$

$$\lambda_{ee} = Z\lambda_{ei}, \tag{6}$$

$E_{g-1/2}$ is the group energy, and Z the material ionization. ξ is an electron-ion collision fix, while the factor r on λ_{ee} emerges from discrepancies amongst SNB implementations in various studies. These adjustments to the mfp definitions are further described in Sec. III.C. of Brodrick et al.[18], where is it suggested that SNB implemented with $r=2$ and $\xi(Z) = (Z+0.24)/(Z+4.2)$, corresponding to the ionization-dependent collision fix first proposed by Epperlein and Short[32], brings SNB predictions in better agreement with VFP modeling.

A number of SNB model variations, relating to the mean free path definitions, are considered in this work and are briefly summarized in Table I. The corrections from Brodrick are implemented in the baseline SNB configuration, referred to as Base-SNB. Additionally, in Base-SNB the effect of electric fields is included via modification to the electron-ion mfp as $1/\lambda'_{g,ei} = 1/\xi\lambda_{g,ei} + 1/\lambda_{g,\mathscr{E}}$, with $\lambda_{g,\mathscr{E}} = E_{g-1/2}/k_BT_e|e\mathscr{E}|$, where $\mathscr{E}(T_e,\ n_e,\ Z)$ is the Spitzer electric field[13]. This adjustment to $\lambda_{g,ei}$ restricts nonlocal deviations from Q_{SH} in regions with strong electric fields, notably in the plasma corona. To assess the effects of the Brodrick's corrections, Base-SNB is compared against SNB with $\xi = 1, r = 1$, referred to as noBR-SNB. In addition, Base-SNB includes a factor of 4 correction to the electron-electron and electron-ion definitions due to differences in electron thermal

TABLE I. Overview of variations in SNB models used, with $\xi = (Z+0.24)/(Z+4.2)$, and Krook collision correction factor $r=2$. The mean free path definitions $\lambda_{g,ee}$, $\lambda_{g,ei}$ correspond to those used in Equation 3, and $\lambda_{g,\mathscr{E}}$ is the Spitzer electric-field correction to the electron-ion mean-free-path.

Name	$\lambda_{g,ee}$	$\lambda'_{g,ei}$
Base	$\lambda_{g0,ee}/r$	$\left[\frac{1}{\xi\lambda_{g0,ei}} + \frac{1}{\lambda_{g,\mathscr{E}}}\right]^{-1}$
noBR	$\lambda_{g0,ee}$	$\left[\frac{1}{\lambda_{g0,ei}} + \frac{1}{\lambda_{g,\mathscr{E}}}\right]^{-1}$
noSL	$\sqrt{\xi\lambda_{g0,ee}\lambda_{g0,ei}}/r$	$\left[\frac{1}{\sqrt{\xi\lambda_{g0,ee}\lambda_{g0,ei}}} + \frac{1}{\lambda_{g,\mathscr{E}}}\right]^{-1}$
noEF	$\lambda_{g0,ee}/r$	$\xi\lambda_{g0,ei}$

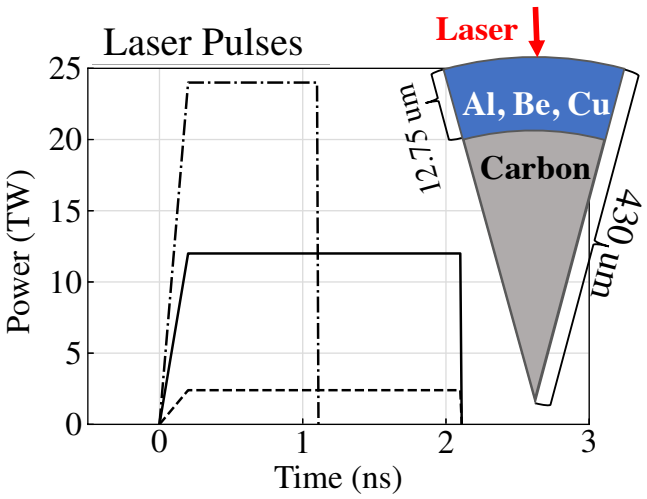

FIG. 1. Pulse shapes used for studying OMEGA equivalent systems, with laser intensities of 1.03 $\times 10^{14}$ W/cm^2 (dashed), 5.2 $\times 10^{14}$ W/cm^2 (solid), and 1.03 $\times 10^{15}$ W/cm^2 (dot-dashed). The sphere is comprised of a solid carbon center, and 12.5 μm coating of material, for which cross-section schematic is overlaid.

velocity definitions between HYDRA and the IMPACT VFP code[33].

Two other model variations are considered in our studies: the first, noSL-SNB, assesses the effect of separated mean free path definitions for electron-electron and electron-ions by employing geometrically averaged mfp $\lambda_g = \sqrt{\xi \lambda_{g,ee} \lambda'_{g,ei}/r}$ for both collision terms in Eqn (3), akin to SNB formulation in the original publication[13]. This treatment assumes constant average ionization Z in the plasma[18,19], while SNB with λ_{ei} and λ_{ee} considered separately appropriately considers ionization gradients present in the plasma profile. The second variant, noEF-SNB, neglects the Spitzer-electric field correction $\lambda_{g,\mathscr{E}}$ to $\lambda_{g,ei}$. This is motivated by previous work that found neglecting the electric field term facilitates better agreement with VFP calculations[19].

B. HYDRA laser-irradiated sphere model

Figure 1 exhibits a cross-section schematic of the laser-irradiated sphere, which has an outer radius of 430 μm. The sphere is solid, so that the nonlocal transport is studied in a relatively steady ablation front. The sphere is comprised of an inner 417.5 μm of solid carbon with density 1 g/cm^3, coated by a 12.5 μm layer of low- to mid-Z material. We consider three materials to assess both the consistency of the SNB model and resulting effects from nonlocal heat fluxes against atomic number: beryllium (Z = 4) with mass density ρ = 1.83 g/cm^3, aluminum (Z = 13) with ρ = 2.7 g/cm^3, and copper (Z = 29) with ρ = 8.96 g/cm^3. The sphere is uniformly irradiated by sixty 351 nm wavelength (3ω) beams, with intensity profile $I(r) = I_o e^{-\left(\frac{r}{r_o}\right)^n}$, where r is the profile radius in microns, $r_o = 358$ μm and $n = 5.2$. In our studies, we consider three laser pulses relevant to ICF conditions, with $I_L = 10^{14} - 10^{15}$ W/cm^2. All three laser pulses are square pulses with 200 ps rise time, and are constrained to conditions relevant to OMEGA experiments. They consist of the following total energy and duration:

- 4.8 kJ in 2 nanoseconds, $I_L \sim 1.03 \times 10^{14}$W/cm^2.
- 24 kJ in 2 nanoseconds, $I_L \sim 5.2 \times 10^{14}$W/cm^2.
- 24 kJ in 1 nanoseconds, $I_L \sim 1.03 \times 10^{15}$W/cm^2.

The 1D-sphere is simulated with the multiphysics radiation hydrodynamics code HYDRA[16]. Radiation transport is modeled using a polar S_N (discrete ordinates) method[34,35] with 24 discrete angles and 60 energy groups. Additionally, simulations were performed using multigroup radiation diffusion, and the effect of the radiation transport method is briefly discussed in section III C. The materials are modeled with tabulated equations of states from LEOS and local-thermodynamic equilibrium opacities (LTE) opacities from OPAL. In the hot, underdense corona the collisional-radiative model DCA[30] is employed to describe the non-LTE atomic kinetics. The threshold for transitioning from LTE tabulated data to the non-LTE DCA model is set at $T_{NLTE} = 100$ eV so that the transition occurs in the dense plasma, and our studies indicate that the simulation is insensitive to the transition at this range. The laser source is modeled as inverse-bremsstrahlung absorption using the spherical laser deposition model in HYDRA. This package is designed to illuminate spheres while producing a minimal amount of statistical noise. The capsule is illuminated with 200 parallel rays equally spaced across the beam width. This accounts for the essential effects of refraction due to the converging capsule geometry. Approximately 2600 Lagrangian zones are used in the simulation domain, which ensures $< 2.5\%$ variation in the laser absorption, coronal T_e and n_e quantities due to resolution effects (see Appendix for details regarding resolution and convergence).

Simulations are performed using flux-limited Spitzer-Harm diffusion over a range of flux-limter factors 0.03-0.20. Simulations with the nonlocal package model thermal transport classically with Spitzer-Harm until the maximum Knudsen number $Kn = \lambda_{ei}/L_T$ in the domain exceeds 0.01, beyond which the electron transport is modeled with SNB nonlocal transport. This threshold is set so that the SNB model is used when nonlocal effects in thermal transport become significant[1], while the Spitzer-Harm transport term is sufficient in the classical regime. In addition, the transition between thermal transport models occurs within the first 50 ps of the 200 ps laser pulse rise, such that $< 1\%$ of the total laser energy deposition in our nonlocal calculations is modeled with Spitzer-Harm transport.

In the SNB multigroup diffusion model, energy groups are discretized with respect to the integral in Equation 4. The first energy bin between E_0 and E_1 is further discretized into "cold groups" evenly spaced in energy, which ensures the rapid rise in the integral is well resolved. In HYDRA's implementation

of SNB, these energy groups are rescaled with the plasma temperature. The present study uses a 20/60 energy group (cold/total) configuration, which is sufficient to converge the heat flux calculation, with the convergence behavior most affected by the number of cold groups.

C. K2 Vlasov-Fokker-Planck model

In these studies, the Vlasov-Fokker-Planck (VFP) code K2[19] is used to calculate kinetic heat fluxes for comparison with SNB modeling. K2 solves the VFP equation for the electron distribution function (EDF) $f(\mathbf{x},\mathbf{p},t)$, expanded in spherical harmonics in momentum-space $(\mathbf{p},\theta,\phi)$. In addition, K2 couples the electron VFP equation to the radiation hydrodynamic equations via heating and cooling operators to account for PdV work and radiative cooling, and through advecting the EDF with hydrodynamic ion motion to maintain quasi-neutrality. Laser energy deposition is modeled by solving the 1D ray equation:

$$\frac{dI(x)}{dx} = -\kappa(x)I(x), \tag{7}$$

with inverse-bremsstrahlung absorption coefficient, $\kappa(x)$, self consistently calculated from energy deposition from the inverse bremsstrahlung heating term C_{IB}[36]. A thorough overview of the VFP model in K2 is detailed in Sherlock et al.[19]

K2 is initiated with electron temperature, density, and ionization plasma conditions on an even spatial grid. The EDF is discretized in velocity space and initiated as a Maxwellian. There is no imposed or generated magnetic field in the 1D spherical geometry, so only the f_0 and f_1 spherical harmonics are used in these calculations, and from the EDF the heat flux is consistently calculated as the v^5 moment of f_1, i.e. $Q_{VFP} \sim \int v^5 f_1(v) dv$. To focus comparisons on the effects of the electron heat flux resulting from the evolution of the EDF, energy transport due to radiation transport and hydrodynamic motion are not considered. Effectively, this constrains comparisons of VFP and SNB heat fluxes to stationary profiles.

III. RESULTS

A. Heat flux calculations in stationary ablation front profiles

We first compare heat flux predictions in the range of plasma conditions generated from HYDRA-SNB modeling. To calculate the K2 heat flux, HYDRA plasma conditions are interpolated onto a 1D spherical K2 mesh to initiate the kinetic calculation. Heating and cooling operators are used to maintain temperature profile as the initial Spitzer-Harm heat flux evolves to the steady state VFP heat flux, defined as when Q_{K2}/Q_{SH} slowly varies in time. Typically, the steady-state EDF and corresponding VFP heat flux is reached in a few electron-ion collision times.

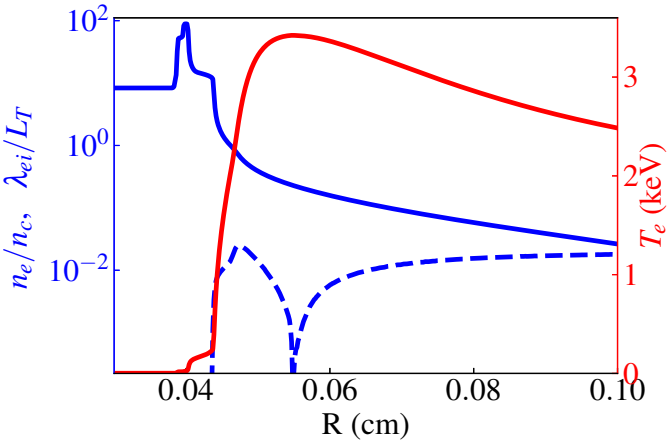

FIG. 2. Electron density (solid blue), electron temperature (solid red), and nonlocality parameter λ_{ei}/L_T (blue dashed) profiles from a copper sphere HYDRA simulation irradiated by 1×10^{15} W/cm^2 square pulse, plotted at t = 1 ns. In this profile, the maximum λ_{ei}/L_T is approximately 0.025 near the critical density.

Figure 2 shows initial plasma conditions generated in a HYDRA-SNB simulation of a copper coated sphere irradiated by a 1 ns 1×10^{15} W/cm^2 square pulse. Given the steep temperature gradients, electron transport is expected to become nonlocal, such that the different models under consideration yield different heat flux predictions. Accordingly, this plasma condition was chosen because the transport was the most nonlocal, and hence the differences between the various heat flux models are largest. However, we note the transport behavior is more significantly affected by the laser intensity, i.e., heat flux predictions from beryllium and aluminum look qualitatively similar each respective laser intensity. The ratio of the electron mean-free-path to temperature gradient length-scale, λ_{ei}/L_T, is shown to illustrate the spatial distribution of nonlocality in the laser-ablation front. In the ablation front near the critical density n_c, λ_{ei}/L_T is ~ 0.025 and is locally maximum, but is comparably important in the hot, underdense coronal region. There is a positive correlation between λ_{ei}/L_T and laser intensity, ~ 0.02 and ~ 0.01 at the same simulation time in copper for the 5×10^{14} W/cm^2 and 1×10^{14} W/cm^2 laser intensities.

The corresponding heat fluxes calculated from the various approaches are shown in Figure 3 for this temperature profile. Compared to the VFP approach, Base-SNB and all the SNB variations overpredict the inward heat flux at the radial position of approximately 470 μm. All approaches agree fairly well with the exception of noBR-SNB, which overpredicts the heat flux by $\sim 60\%$, while the other SNB configurations are about 15% larger. SNB as a whole is a significant improvement over the local heat flux, which overpredicts K2-VFP by 150%.

In the corona region, the predicted heat flux is more strongly affected by the mean-free-path definitions in the SNB model variations. Neglecting the electric field term in noEF-SNB reduces the heat flux slightly by enabling the

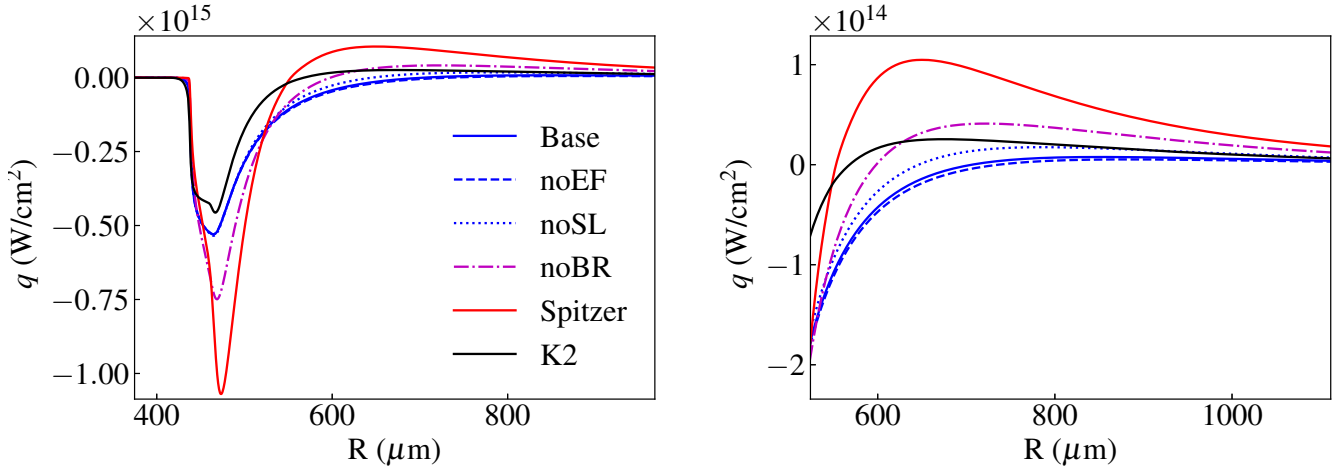

FIG. 3. Heat fluxes in the (a) ablation front and (b) focused on the corona region for the initial conditions modeled in Fig. 2. Black: K2-VFP, red : Spitzer-Harm, green: noBR-SNB, solid-blue: Base-SNB, dashed-blue: noEF-SNB, dotted-blue: noSL-SNB. The peak nonlocal heat flux is reduced (at about 450 μm) from the classical Spitzer-Harm local heat flux. Of the SNB models, those with the corrections suggested by Brodrick et al exhibited the best agreement with Fokker-Planck calculations. (b) Heat fluxes in the corona region, which are also reduced. Here, the SNB heat flux shows larger sensitivities to the model variations.

transport to become more nonlocal, while the opposite effect is observed in SNB using an averaged mfp (noSL-SNB). Similar to the ablation front, noBR-SNB predicts a much larger heat flux compared to the other model variations. Figure 3(b) shows the heat fluxes for the different transport models in the corona region. In the corona, K2 predicts a reduced heat flux, with peak coronal heat flux approximately 4 times smaller ($Q_{VFP} \sim 0.25 \times 10^{14}$ W/cm^2, $Q_{SH} \sim 1 \times 10^{14}$ W/cm^2) than the local heat flux. Clearly in the corona, none of the heat fluxes agree with K2-VFP modeling. The magnitude of the coronal heat fluxes appear most similar between K2-VFP and noBR-SNB; however, as previously observed this is at the expense of the agreement in the ablation region. Notwithstanding, all the SNB models qualitatively produce the coronal heat flux limitation indicated by the K2-VFP calculation.

We also examine the inward preheat predicted beyond the steep temperature front. Fig 4(a) shows the heat fluxes at the ablation region, with the electron temperature indicated by the light red line. At the end of the steep temperature front at $\sim$ 150 eV, the lower electron temperatures and smoother temperature gradients substantially reduces the Spitzer-Harm heat flux. Here, K2-VFP exhibits the longest range preheating, while noBR-SNB predicts the shortest range preheating. Fig. 4(b) inspects the electron distribution function f_0 from K2 taken at $r = 420$ μm from the temperature profile in Fig4(a). Compared to the Maxwellian distribution, the K2-VFP electron distribution has a broad secondary distribution of high-energy electrons, with mean energy $\sim$ 8.7 keV. A simple estimate of the mean free path of these high-energy electrons can be made from Equation 1 using the local plasma conditions, which are $n_e = 1.2 \times 10^{23}$ cm^{-3}, $Z = 18$, and $\ln\Lambda_{ei} \approx 2.1$, yielding mfp $\lambda_{ei} = 5\mu$m. This is consistent with the length of the preheat region.

Similar behavior is observed in stationary profiles from beryllium and aluminum simulations. Specifically, we observe disagreements in the coronal heat fluxes, and consistently longer range preheating by K2-VFP than any of the SNB model variations. In addition, noBR- and noEF-SNB are consistently close to the baseline SNB model, with small differences in the coronal heat fluxes. With respect to the laser intensity, relative errors between VFP and SNB heat fluxes are smaller at the lower laser intensities, but the departure from the classical Spitzer-Harm heat flux is smaller as well. Magnitudes of peak heat fluxes in the ablation region are summarized in Figure 5, which shows the percent difference of the peak HYDRA-SNB heat fluxes with respect to K2-VFP heat flux for the Base-SNB and noBR-SNB configurations. NoSL-SNB and noEF-SNB predict the same heat flux as Base-SNB. This panel shows the Brodrick corrections incorporated in the Base-SNB model substantially improves agreement with K2-VFP heat flux predictions, reducing the difference to K2-VFP from 60% to <20% at 10^{15} W/cm^2 laser intensity, and essentially agreeing at lower laser intensities. Furthermore, these adjustments result in more consistent performance across the range of materials (and ionizations) in our studies, while the noBR-SNB model exhibits increased errors with Z, which constrains the range of applicability.

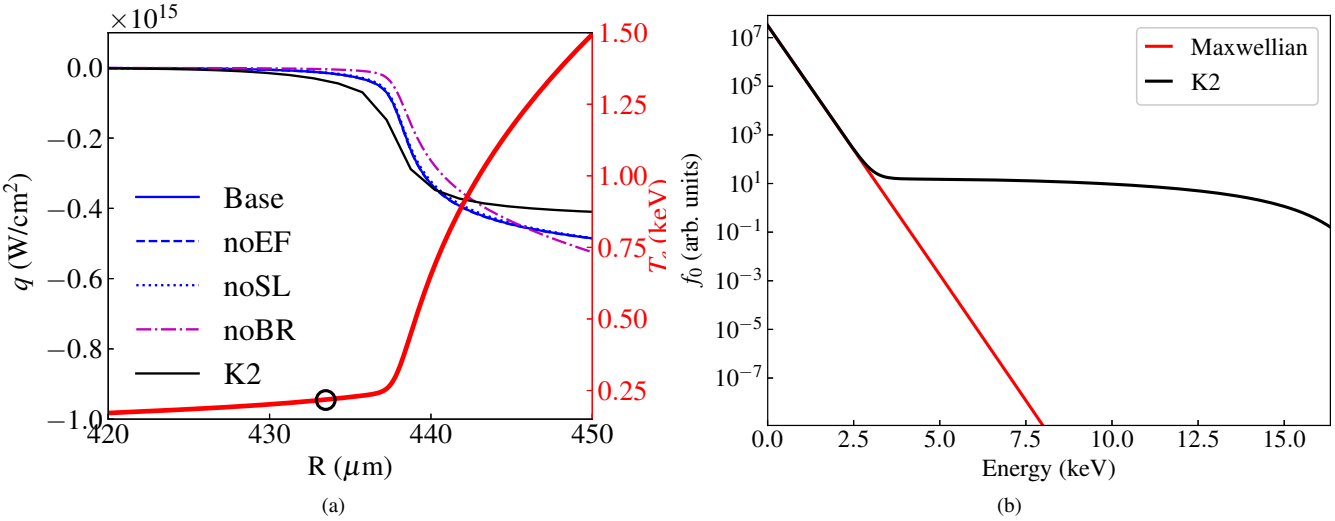

FIG. 4. (a) Heat flux profiles in the preheat region of the plasma from the electron temperature profile (red) given in Fig 2. SNB predicts shorter-range preheating than K2. (b) K2 (black) and Maxwellian (red) electron distribution functions (EDFs) f_0 plotted against the electron energy (in keV) from the plasma at radius r = 420 μm, indicated by the symbol in (a). The high energy population of electrons here is due to the nonlocal preheating.

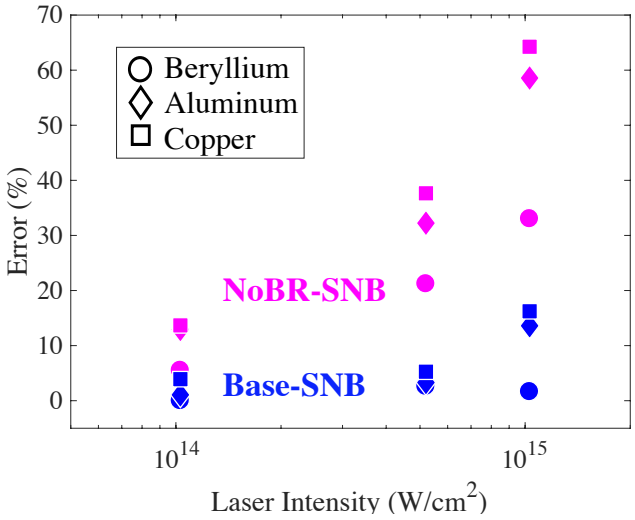

FIG. 5. Heat flux differences of noBR SNB and Base SNB when compared to K2 (VFP), for different laser intensities in Be, Al, and Cu-spheres. With the corrections suggested by Brodrick et al., the accuracy of the SNB nonlocal model as well as consistency across different materials is increased. All comparisons are made at $t = 1$ ns, when the laser-plasma ablation front is well developed.

B. Inline temperature evolution

While SNB heat fluxes in the ablation region exhibit good agreement with K2-VFP calculations, we did observe differences in heat flux predictions in the preheating region (where K2-VFP predicts longer range preheating than SNB), and a general lack of correlation in the coronal region. It is important to determine how these aspects of the heat flux predictions may propagate to the temperature profile. To do so, we consider a more direct comparison between the VFP and SNB models by simulating the evolution of two temperature profiles: one with K2-VFP heat fluxes, and the other with heat fluxes from the kinetic SNB model implemented in K2[19], which is equivalent to the $r = 2$ Base-SNB model. The test problem consists of a beryllium plasma, irradiated by a 3ω-square pulse with 100 ps rise time and peak intensity of 5×10^{14} W/cm^2 intensity using K2's laser energy deposiition model. The initial electron density and ionization conditions are shown in Figure 6. The beryllium is modeled as fully ionized (Z = 4), while the electron density profile is exponential with gradient scale length $L_{n_e} \sim 200\mu$m, which assumes the plasma expanded isothermally[37]. The electron densities in the domain spans the absorption region and underdense corona, with electron densities ranging from $(0.001 - 2)n_c$. The plasma temperatures rise in time, with $T_e \sim 2.9$ keV at 500 ps.

In this test, the evolving temperature profiles highlight the effect of differences in SNB and VFP heat fluxes. K2-VFP and K2-SNB electron temperatures are shown at different times in Figure 7 to show how the two temperature profiles evolve over the duration of the laser-heating. The maximum electron temperature of the two profiles at (0.1-0.3)n_c rises in a similar fashion. In the innermost region, the K2-SNB heat flux is larger and the temperature front advances further into the dense plasma than the front from K2-VFP. In the K2 simulation this effect is exaggerated because the density profile is still exponential beyond n_c, while the density gradients are much sharper beyond n_C in the sphere profiles, which leads to a more collisional plasma. In the corona region, electron temperatures from K2-VFP modeling is greater than K2-SNB, which corresponds to the larger coronal heat flux observed from stationary profile comparisons. However, these

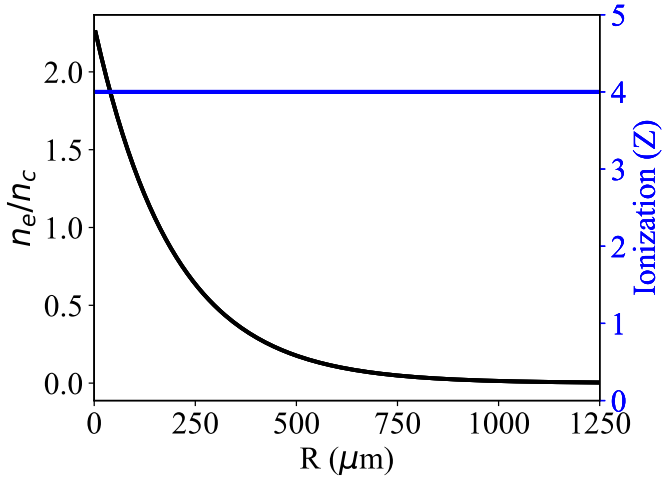

FIG. 6. Initial normalized electron density n_e/n_c (black) and material ionization Z (blue) for K2 beryllium sphere temperature evolution simulation, irradiated at 5×10^{14} W/cm^2 laser intensity.

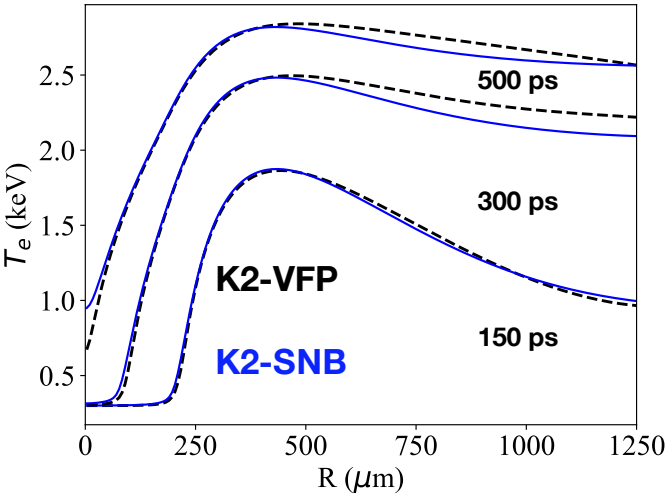

FIG. 7. Electron temperatures for K2-VFP (black-dashed) and K2-SNB (blue) temperature profiles plotted at 150 ps, 300 ps, and 500 ps. In the low-density corona, the electron temperatures remain fairly close for the duration of the temperature-evolution test.

differences are relatively small, on the order of 50-75 eV or 2-3% at the end of the laser heating. In addition, the temperatures are closer to each other than at t = 300 ps, where K2-SNB is cooler by 100-150 eV. The convergence of coronal temperatures indicates that that small errors in the heat flux are self-correcting: If the heat flux is too small, the temperature gradient steepens. Subsequently, the steeper temperature gradients result in a larger heat flux.

C. Implications for experiments

Stationary profile heat flux comparisons between the SNB model and K2 showed that the SNB model implemented with $r = 2, \xi = (Z+0.24)/(Z+4.2)$ agree well with kinetic heat

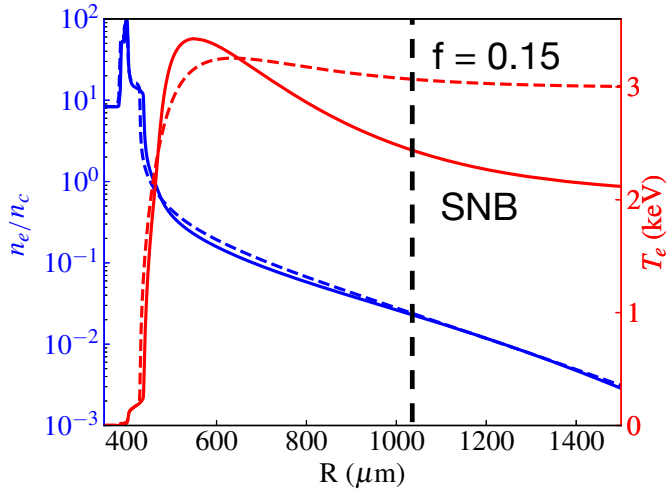

FIG. 8. T_e (red) and n_e (blue) profiles from HYDRA Cu-sphere simulations at 1×10^{15} W/cm^2 laser intensity and t = 1 ns for $f = 0.15$ Spitzer-Harm (dashed lines) and Base-SNB (solid lines) electron transport models. The nonlocal plasma coolrs more significantly as it expands, and is much cooler than $f = 0.15$ in the underdense corona (dashed black line).

fluxes, notably in the important ablation region near n_C. The inline simulation of an irradiated beryllium sphere modeled with the K2-VFP and K2-SNB heat fluxes indicated that the resulting temperature profile did not differ significantly between the two transport approaches despite the observed discrepancies in heat fluxes. In this section, the SNB model is considered in full radiation-hydrodynamics HYDRA simulations, from which we assess how differences from SNB nonlocal heat fluxes propagate to the experimental observables when compared to flux-limited Spitzer-Harm, i.e., local diffusion, in HYDRA simulations. Though the flux limiter is an *ad hoc* approach, it is still worthwhile to determine if nonlocal transport effects can be reasonably modeled with an appropriate value of f. Similar work showed that at these laser intensities ($10^{14} - 10^{15}$ W/cm^2), an initial flux limiter with $f \sim 0.09$ at early time and subsequently decreased to $f \sim 0.06$ over the duration of a 1 ns laser pulse reasonably matches experimental measurements from direct-drive planar foil acceleration experiments[38]. As the goal of this work is to assess nonlocal transport effects in the SNB model, relevant comparisons are constrained against HYDRA modeling with constant f Spitzer-Harm as opposed to exploring time-dependent sensitivities.

It is expected that the heat flux modeling will affect the development of the ablation front, which dictates the radial electron temperature and density profiles at a given time. Figure 8 shows T_e, n_e plasma conditions from copper sphere HYDRA simulations at 10^{15} W/cm^2 laser intensity, evolved with $f = 0.15$ Spitzer-Harm and Base-SNB nonlocal transport models plotted at t = 1 ns. At electron densities near n_c, the nonlocal plasma is hotter with peak electron temperature of ~3.5 keV at radius 550 μm compared to ~3.2 keV for the $f = 0.15$ Spitzer-Harm result. The hotter temperatures here result from weaker cooling due to reduced ablation

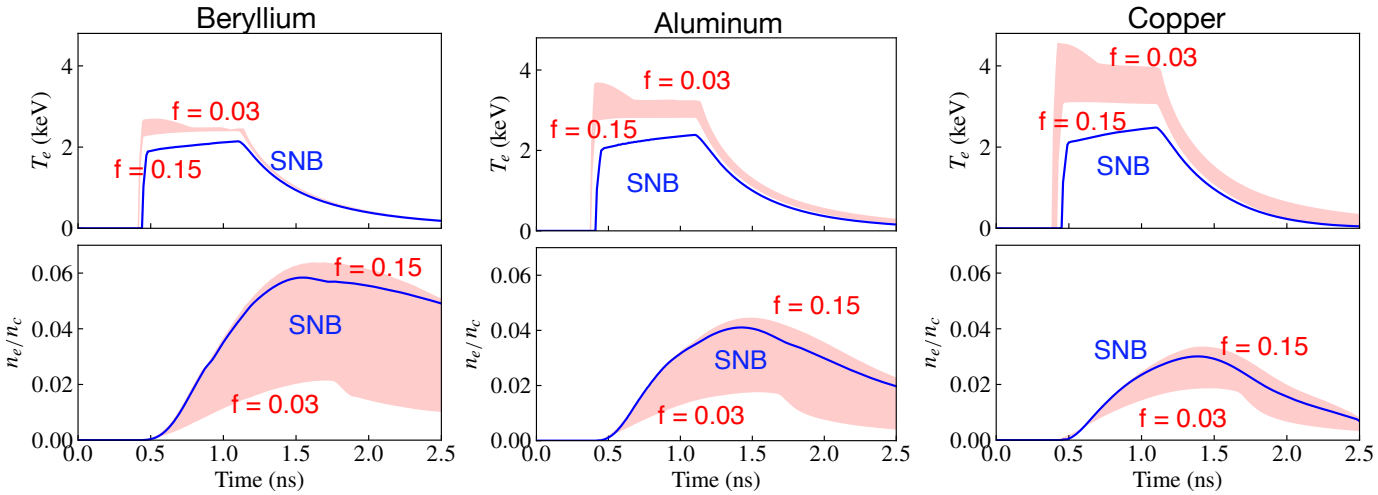

FIG. 9. Inferred time-dependent coronal T_e, n_e from HYDRA simulations at 1×10^{15} W/cm^2 laser intensity, taken at position $r = 1030$ μm for beryllium, aluminum, and copper. The red, shaded region encompasses the range of flux-limited Spitzer-Harm modeling with $f = 0.03 - 0.15$, while the solid-blue line is the HYDRA-SNB result. HYDRA-SNB coronal electron temperatures are consistently cooler than their Spitzer-Harm counterparts.

heat fluxes from the nonlocal model (as shown in Figure 3). Similar to low f flux-limited Spitzer-Harm simulations, the Base-SNB simulation exhibits a sharper density decrease near n_c, characteristic of flux-limited heat transport in the ablation region, leading to lower electron densities in the coronal region with increasing radius. Ostensibly, the larger density gradients near n_C and hotter electron temperatures increases the laser scattering in the copper plasma. However this effect is relatively small, only reducing the laser-coupling from 99% to 95% in the Base-SNB. The largest difference in laser absorption is observed in beryllium simulations at 10^{15} W/cm^2 intensity, where the total coupled energy is reduced from 90% to 75%. For lower laser intensities, the corresponding classical and nonlocal absorptions are closer to unity, and the same at 10^{14} W/cm^2 where nonlocal transport effects are observed to be negligible. With respect to plasma density and laser absorption, we find that $f = 0.09$ Spitzer-Harm reasonably matches the range of laser-coupling and electron density profiles produced with the nonlocal transport model. However, $f = 0.09$ Spitzer-Harm transport does not produce the cooler nonlocal coronal electron temperatures. In fact, HYDRA-SNB coronal temperatures are consistently cooler than Spitzer-Harm modeling with any degree of flux-limitation. As the heated plasma expands outwards it cools from PdV work. However, in $f = 0.15$ Spitzer-Harm calculations the cooling is mitigated by strong coronal heat fluxes out into the expanding plasma, enabling an isothermal expansion. In the Base-SNB HYDRA simulation, the coronal heat flux is reduced by nonlocality and insufficiently heats the cooling plasma during expansion. This effect is more significant farther out in the underdense corona, at lower electron densities (<0.1n_c) where the expanding plasma does not couple to the incoming laser.

In an experiment, the cooler coronal temperatures can be identified by a time-resolved optical Thomson Scattering diagnostic[39] placed at the appropriate radial position to probe the coronal density and temperature conditions. Once the laser-ablation front reaches a steady state, the free expansion of the irradiated plasma can be reasonably approximated as a self-similar isothermal rarefaction in spherical geometry, for which the density profile is described as $n_e(r) \sim \exp(-r/L_{n_e})$, where the density gradient scale length $L_{n_e} = c_S t/\sqrt{3}$ with plasma sound speed $c_S \propto (ZT_e/M)^{0.5}$[40]. At 10^{15} W/cm^2, c_S ranges from 350-400 μm/ns for the different materials, and we find it is relatively insensitive to f. The corresponding plasma scale length is $L_{n_e} \sim 200$ μm at t = 1 ns, and so we elect to place a probe 600 μm (or approximately three inverse e-foldings) away from the initial outer radius to ensure the simulated measurement probes electron densities below $0.1n_c$, i.e. in sufficiently underdense plasma where the 351 nm driving laser does not signficantly couple to the expanding plasma. For spheres at lower laser intensities, this position may be too far out in the corona, as the plasmas are cooler and so the corresponding expansion velocities are slower. Fortunately, given a reasonable estimate for the plasma temperature an equivalent probe position can be readily calculated.

Figure 9 shows the corresponding inferred n_e and T_e values at a probe placed 600 μm from the initial sphere (r = 1030 μm) over time, corresponding to the position indicated by the dashed-black line in Figure 8 for beryllium, aluminum, and copper at the 1×10^{15} W/cm^2 laser intensity where the nonlocal effects are most significant. For each material, the low-density tail of the expanding plasma reaches the probe position at about the same time for all the simulations, indicating that the plasma expands at similar velocities between different treatments for the electron thermal transport. Electron densities from Spitzer-Harm

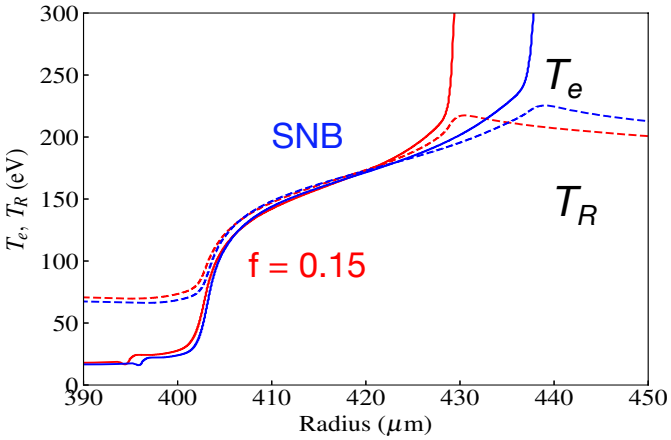

FIG. 10. T_e (solid lines) and T_R (dashed lines) profiles in the radiation flux dominated region of the ablation front for HYDRA copper spheres at 1×10^{15} W/cm^2 laser intensity and t = 1 ns for $f = 0.05$ (red) Spitzer-Harm transport models, and Base-SNB (blue). The SNB Marshak temperature front is larger than the $f = 0.15$ Spitzer-Harm temperature front.

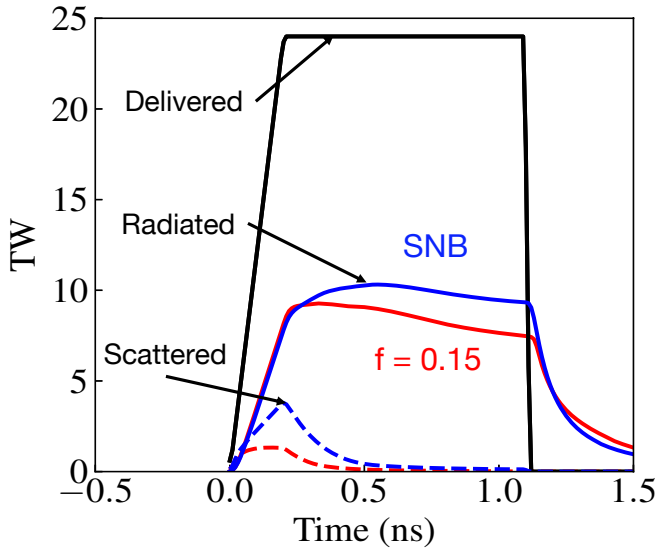

FIG. 11. Emitted X-ray power (solid lines) and scattered laser power (dashed lines) vs. time for copper sphere simulations at 1×10^{15} W/cm^2 laser intensity for $f = 0.15$ (red) Spitzer-Harm transport, and Base-SNB (blue) HYDRA simulations for the 24 TW square pulse (black line). X-ray flux from the SNB nonlocal model is greater (∼10 Terawatts) than X-ray emissions with Spitzer-Harm electron transport modeling (∼7.5-9 Terawatts).

modeling are lowest for highly flux-limited calculations ($f = 0.03$). These lower ablation densities reflect two effects: the reduced expansion of the heated material beyond n_c, and a stronger, sharper decompression at the critical surface before the subsequent free expansion. Coronal densities are highest for beryllium, which is consistent with the Z^{-1} scaling of thermal conduction in the ablation region, which correlates to the expansion of the dense material. Due to this scaling, beryllium electron densities are more sensitive to the thermal transport model than aluminum and copper materials. Overall, Base-SNB nonlocal densities fall within the range of flux-limited Spitzer-Harm modeling indicated by the shaded region, correlating to moderate flux-limitation of the heat flux in the ablation region. In contrast, differences in coronal temperatures can be clearly observed at the probe position. The largest temperature differences can be observed in copper, where HYDRA-SNB simulations give temperatures from 2.0-2.4 keV, while the coolest Spitzer-Harm modeling predicts temperatures $\sim$ 3.0 keV. However, we note that in lower-Z materials overall electron temperatures are less sensitive to the thermal transport modeling and the cooler coronal temperatures are still a distinct feature.

In addition to utilizing a Thomson scattering probe, nonlocal transport effects in aluminum and copper laser-irradiated spheres can also be probed by measuring the emitted X-ray power. In simulations for the mid-Z materials, a non-negligible fraction of the absorbed laser energy is re-emitted as thermal radiation, in contrast to the lower-Z beryllium where only 5% of the absorbed laser energy is converted to X-ray power. In the ablation front, some of the laser light absorbed in the corona is converted into X-rays, which radiate equally into the dense plasma and out into the corona region. The radiation in the dense plasma couples strongly to the material in the mid-Z materials, forming a relatively low temperature diffusive thermal front that re-emits thermal radiation out into the underdense corona. As the electron temperature is much lower in this region it is dominated by the radiation transport, and the end result is a double temperature front, i.e. double ablation front[41]. Figure 10 shows electron and radiation temperatures in the low temperature foot for $f = 0.15$ Spitzer-Harm and Base-SNB simulations, where the similar temperatures are indicative of the strong radiative and material energy coupling. In Figure 4, the Spitzer-Harm heat fluxes in this region fall off significantly due to the lower temperatures and smoother gradients, while SNB heat fluxes predict preheating into the absorption layer. In the time-integrated simulations, this yields a larger and hotter Marshak wave from theBase-SNB calculation. Essentially, the preheat enables the delivery of more energy via additional electron thermal transport from the laser-absorption region to the radiation-dominated region. Consequently, the emitted radiative power in the nonlocal plasma increases. Figure 11 shows the X-ray emissions and total laser scattering over time for copper at 10^{15} W/cm^2 laser intensity for the Base-SNB and f = 0.15 Spitzer-Harm thermal conduction models, illuminated by the 1 ns, 24 TW peak power square pulse. The emitted X-ray power from the $f = 0.15$ simulation is the largest possible radiation flux obtained from Spitzer-Harm modeling, starting at 9 TW and reducing to 7.5 TW right before the end of the pulse. In contrast, the HYDRA Base-SNB simulation presents larger radiation heat fluxes (about 10 TW throughout the pulse duration) than the range of Spitzer-Harm modeling.

In addition to the S_N transport calculations, all previous studies (using both the classical and reduced nonlocal electron

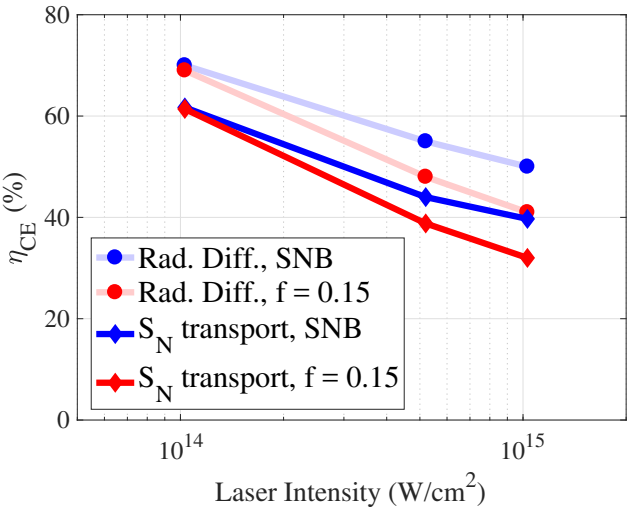

FIG. 12. Conversion efficiency $\eta_{CE} = P_R/(P_{laser} - P_{backscatter})$, plotted against $\log_{10}(I_L)$, for copper spheres modeled with the Base-SNB (blue) and $f = 0.15$ (red) Spitzer-Harm thermal transport models, and with multigroup radiation diffusion (light lines) and S_N radiation transport (dark lines) models. With increasing laser intensity, nonlocal electron transport recovers more and more conversion efficiency, independent of the radiation transport method.

transport models) were also simulated with flux-limited radiation-diffusion using the same energy group structure. It is found that in the coronal region, the observed electron temperatures and densities are consistent between polar S_N and radiation diffusion methods, notably with the same coronal temperature differences between classical and nonlocal electron transport. Differences between these HYDRA simulations manifested primarily in the Marshak wave region (as shown in Fig. 10 for copper), whose structure exhibited sensitivities to the choice of radiation transport model. However, we note that in HYDRA simulations with both radiation transport models, the SNB thermal front was longer and hotter than the corresponding Spitzer-Harm temperature front.

Accordingly, the differences in the Marshak front propagates to the emitted radiation flux. Figure 12 shows the corresponding X-ray conversion efficiency η_{CE} for copper as a function of laser intensity for the $f = 0.15$ Spitzer-Harm and Base-SNB electron conduction models, as well as the S_N and flux-limited diffusion radiation transport models. η_{CE} is defined as (P_R/P_{abs}), where P_{abs} is the absorbed laser power, and P_R is the emitted X-ray power. Here, all values are calculated at $t = 1$ ns. Clearly, as the laser intensity increases and the electron transport becomes increasingly nonlocal, the conversion efficiency increases as well.

It is evident that the increased radiation emission due to electron preheating in both S_N transport and multigroup diffusion HYDRA simulations. The primary observed difference between simulations with different radiation transport methods is an increase in the η_{CE} by about 10% relative from multigroup radiation diffusion compared to the S_N method. A similar difference in conversion efficiency is observed in aluminum sphere simulations: At 1×10^{15} W/cm^2 laser intensity and with multigroup radiation diffusion, $\eta_{CE} \sim 30\%$ and 25% for SNB and SH electron conduction (at 1×10^{15} W/cm^2). From S_N transport simulations, $\eta_{CE} \sim 20\%$ and 16% respectively for the reduced-nonlocal and classical electron conduction models.

IV. CONCLUSIONS

The SNB nonlocal electron transport model was evaluated in laser-irradiated spheres across a range of materials and at intensities relevant to laser ICF experiments ($10^{14} - 10^{15}$ W/cm^2). We find for the plasma conditions produced in direct-drive spheres at these laser intensities the SNB electron heat fluxes present good agreement with Fokker-Planck predictions from the K2 code. Heat flux comparisons show the baseline HYDRA SNB model that incorporates corrections from Brodrick[18] reduces the heat flux error to 15% at the highest laser intensity of 10^{15} W/cm^2, in contrast with $\sim 60\%$ disagreement without these improvements. In the preheat region, all variations of the SNB model underpredict the range of the preheat compared to K2, while in the coronal region the SNB and K2 heat fluxes generally disagree. However, a temperature evolution test between the K2-SNB and K2 Fokker-Planck heat fluxes indicate that the resulting effect on from these heat flux discrepancies on the plasma temperature is small. These comparisons to experimentally relevant simulations corroborate the conclusions presented by Brodrick et al[18].

In radiation-hydrodynamics HYDRA simulations of the laser-irradiated sphere, nonlocal transport effects on the plasma evolution have been identified, and can be observed by probing the coronal plasma conditions, and in mid-Z materials by measuring the emitted X-ray power. In additon, observed differences in measurable quantities can be related to different aspects of the nonlocal transport: reduced laser energy coupling and electron densities indicate reduced heat flux in the dense plasma, while cooler coronal temperature indicate reduced heat flux in the underdense corona. Furthermore, increased X-ray emissions provide evidence of preheating in the plasma at densities above n_c. While some of these measurable effects (laser-coupling and coronal electron densities) can be reasonably approximated with flux-limited Spitzer-Harm, lower coronal electron temperatures and higher X-ray energy fluxes predicted by the SNB model fall beyond the range of Spitzer-Harm modeling. These model predictions can and should be tested by experiments.

ACKNOWLEDGMENTS

The authors acknowledge helpful conversations with H.P. Le, G.F. Swadling, G.D. Kerbel, M.M. Marinak, and C.P. Ridgers.

This document was prepared as an account of work sponsored by an agency of the United States government. Neither the United States government nor the Lawrence

This work is supported by the Lawrence Livermore National Laboratory under subcontract B614207, and was performed under the auspices of the U.S. Department of Energy by Lawrence Livermore National Laboratory under Contract No. DE-AC52-07NA27344.

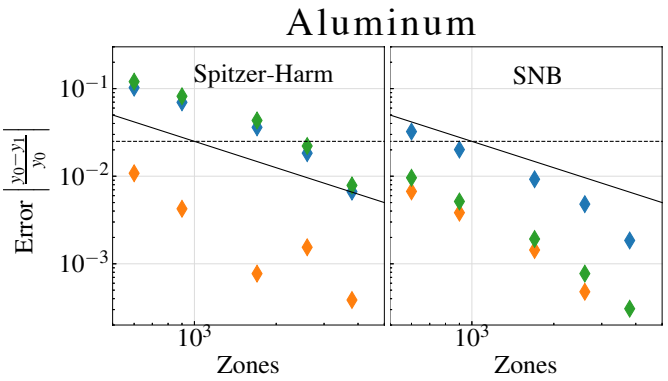

FIG. 13. Electron temperature (orange) and density (blue) convergence results at $r = 820$ μm at $t = 1$ ns as well as total energy coupling (green) for aluminum spheres simulations using the (left) Spitzer-Harm ($f = 0.05$) and (right) SNB electron thermal transport models. The error percentage is the normalized deviation from the highest resolution calculations. Solid black line: linear convergence rate; dashed black line: 2.5% error.

Appendix: Numerical convergence of the 1D sphere

The irradiated plasma develops into an ablation front composed of two regions separated by the critical density. During the simulation, the strong laser energy deposition in the radial region near the critical density develops strong T_e and n_e gradients that can span a few numerical zones, so we present a convergence study of the simulations to constrain our observations. The feather ratio R is varied such that the total radial zones ranged from ~ 600 to ~ 4800 zones in the coarsest and finest resolution simulations. We quantify the convergence by the variation of the instantaneous coronal electron temperatures and densities at $t = 1$ ns, taken $r = 820$ μm or 390 μm from the initial sphere surface, as well as in the integrated quantity of total laser energy absorption during the simulation duration. The relative variation in T_e, n_e and laser absorption is calculated as $\varepsilon = \left|\frac{y_0-y_1}{y_0}\right|$, where y_0 is from a maximum resolution 1D simulation using 4800 Lagrangian zones. Figure 13 shows the convergence behavior in observables from aluminum spheres, which exhibits the largest error of the materials under consideration. The convergence behavior is close to first-order, i.e., $\varepsilon \propto N^{-1}$ where N is the number of zones. HYDRA SNB simulations exhibit significantly smaller errors. For an error of $\varepsilon < 0.025$ in T_e, n_e and laser absorption, $f = 0.05$ Spitzer-Harm HYDRA simulations require ~ 2600 Lagrangian zones, while SNB simulations require ~ 900 Lagrangian zones. From these studies, $\sim$2600 zones are used to ensure $< 2.5\%$ variation in laser absorption, coronal T_e and n_e due to resolution effects.

[1] A. R. Bell, R. G. Evans, and D. J. Nicholas, Phys. Rev. Lett. **46**, 243 (1981).
[2] R. Kidder, Nucl. Fusion **21**, 145 (1981).
[3] L. Spitzer and R. Härm, Phys. Rev. **89**, 977 (1953).
[4] O. S. Jones, L. J. Suter, H. A. Scott, M. A. Barrios, W. A. Farmer, S. B. Hansen, D. A. Liedahl, C. W. Mauche, A. S. Moore, M. D. Rosen, J. D. Salmonson, D. J. Strozzi, C. A. Thomas, and D. P. Turnbull, Phys. Plasmas **24** (2017).
[5] M. Rosen, H. Scott, D. Hinkel, E. Williams, D. Callahan, R. Town, L. Divol, P. Michel, W. Kruer, L. Suter, R. London, J. Harte, and G. Zimmerman, High Energy Density Phys. **7**, 180 (2011).
[6] R. S. Craxton, K. S. Anderson, T. R. Boehly, V. N. Goncharov, D. R. Harding, J. P. Knauer, R. L. McCrory, P. W. McKenty, D. D. Meyerhofer, J. F. Myatt, A. J. Schmitt, J. D. Sethian, R. W. Short, S. Skupsky, W. Theobald, W. L. Kruer, K. Tanaka, R. Betti, T. J. Collins, J. A. Delettrez, S. X. Hu, J. A. Marozas, A. V. Maximov, D. T. Michel, P. B. Radha, S. P. Regan, T. C. Sangster, W. Seka, A. A. Solodov, J. M. Soures, C. Stoeckl, and J. D. Zuegel, Phys. Plasmas **22** (2015).
[7] W. Seka, D. H. Edgell, J. P. Knauer, J. F. Myatt, A. V. Maximov, R. W. Short, T. C. Sangster, C. Stoeckl, R. E. Bahr, R. S. Craxton, J. A. Delettrez, V. N. Goncharov, I. V. Igumenshchev, and D. Shvarts, Phys. Plasmas **15**, 056312 (2008).
[8] T. R. Boehly, D. Munro, P. M. Celliers, R. E. Olson, D. G. Hicks, V. N. Goncharov, G. W. Collins, H. F. Robey, S. X. Hu, J. A. Morozas, T. C. Sangster, O. L. Landen, and D. D. Meyerhofer, Phys. Plasmas **16** (2009).
[9] S. G. Glendinning, S. N. Dixit, B. A. Hammel, D. H. Kalantar, M. H. Key, J. D. Kilkenny, J. P. Knauer, D. M. Pennington, B. A. Remington, R. J. Wallace, and S. V. Weber, Phys. Rev. Lett. **78**, 3318 (1997).
[10] D. Cao, G. Moses, and J. Delettrez, Phys. Plasmas **22**, 082308 (2015).
[11] V. N. Goncharov, T. C. Sangster, P. B. Radha, R. Betti, T. R. Boehly, T. J. B. Collins, R. S. Craxton, J. A. Delettrez, R. Epstein, V. Y. Glebov, S. X. Hu, I. V. Igumenshchev, J. P. Knauer, S. J. Loucks, J. A. Marozas, F. J. Marshall, R. L. McCrory, P. W. McKenty, D. D. Meyerhofer, S. P. Regan, W. Seka, S. Skupsky, V. A. Smalyuk, J. M. Soures, C. Stoeckl, D. Shvarts, J. A. Frenje, R. D. Petrasso, C. K. Li, F. Seguin, W. Manheimer, and D. G. Colombant, Phys. Plasmas **15**, 056310 (2008).
[12] J. F. Luciani, P. Mora, and J. Virmont, Phys. Rev. Lett. **51**, 1664 (1983).
[13] G. P. Schurtz, P. D. Nicolaï, and M. Busquet, Phys. Plasmas **7**, 4238 (2000).
[14] W. Manheimer, D. Colombant, and V. Goncharov, Phys. Plasmas **15** (2008).
[15] G. Schurtz, S. Gary, S. Hulin, C. Chenais-Popovics, J.-C. Gauthier, F. Thais, J. Breil, F. Durut, J.-L. Feugeas, P.-H. Maire, P. Nicolaï, O. Peyrusse, C. Reverdin, G. Soullié, V. Tikhonchuk, B. Villette, and C. Fourment, Phys. Rev. Lett. **98**, 095002 (2007).
[16] M. M. Marinak, G. D. Kerbel, N. A. Gentile, O. Jones, D. Munro, S. Pollaine, T. R. Dittrich, and S. W. Haan, Phys. Plasmas **8**, 2275 (2001).
[17] A. Marocchino, M. Tzoufras, S. Atzeni, A. Schiavi, P. D. Nicolaï, J. Mallet, V. Tikhonchuk, and J. L. Feugeas, Phys. Plasmas **20** (2013).
[18] J. P. Brodrick, R. J. Kingham, M. M. Marinak, M. V. Patel, A. V. Chankin, J. T. Omotani, M. V. Umansky, D. Del Sorbo, B. Dudson, J. T. Parker, G. D. Kerbel, M. Sherlock, and C. P. Ridgers, Phys. Plasmas **24**, 092309 (2017).

[19]M. Sherlock, J. P. Brodrick, and C. P. Ridgers, Phys. Plasmas **24**, 082706 (2017).
[20]D. Del Sorbo, J. L. Feugeas, P. Nicolaï, M. Olazabal-Loumé, B. Dubroca, S. Guisset, M. Touati, and V. Tikhonchuk, Phys. Plasmas **22** (2015).
[21]W. C. Mead, E. M. Campbell, K. G. Estabrook, R. E. Turner, W. L. Kruer, P. H. Lee, B. Pruett, V. C. Rupert, K. G. Tirsell, G. L. Stradling, F. Ze, C. E. Max, and M. D. Rosen, Phys. Rev. Lett. **47**, 1289 (1981).
[22]E. L. Dewald, M. Rosen, S. H. Glenzer, L. J. Suter, F. Girard, J. P. Jadaud, J. Schein, C. Constantin, F. Wagon, G. Huser, P. Neumayer, and O. L. Landen, Phys. Plasmas **15**, 072706 (2008).
[23]J. J. Thomson, W. L. Kruer, G. J. Caporaso, V. C. Rupert, W. C. Mead, D. W. Phillion, H. N. Kornblum, K. G. Tirsell, V. W. Slivinsky, M. J. Boyle, and M. D. Rosen, Phys. Fluids **22**, 2020 (2003).
[24]P. Alaterre, H. Pépin, R. Fabbro, and B. Faral, Phys. Rev. A **34**, 4184 (1986).
[25]R. J. Henchen, M. Sherlock, W. Rozmus, J. Katz, D. Cao, J. P. Palastro, and D. H. Froula, Phys. Rev. Lett. **121**, 125001 (2018).
[26]P. D. Goldstone, S. R. Goldman, W. C. Mead, J. A. Cobble, G. Stradling, R. H. Day, A. Hauer, M. C. Richardson, R. S. Marjoribanks, P. A. Jaanimagi, R. L. Keck, F. J. Marshall, W. Seka, O. Barnouin, B. Yaakobi, and S. A. Letzring, Phys. Rev. Lett. **59**, 56 (1987).
[27]T. Mochizuki, T. Yabe, K. Okada, M. Hamada, N. Ikeda, S. Kiyokawa, and C. Yamanaka, Phys. Rev. A **33**, 525 (1986).
[28]R. P. Drake, K. G. Estabrook, H. A. Baldis, S. H. Batha, K. S. Bradley, and R. J. Procassini, Phys. Rev. Lett. **73**, 2055 (1994).
[29]J. A. Stamper, K. Papadopoulos, R. N. Sudan, S. O. Dean, E. A. McLean, and J. M. Dawson, Phys. Rev. Lett. **26**, 1012 (1971).
[30]H. Scott and S. Hansen, High Energy Density Phys. **6**, 39 (2010).
[31]E. M. Epperlein, R. W. Short, and A. Simon, Phys. Rev. Lett. **69**, 1765 (1992).
[32]E. M. Epperlein and R. W. Short, Phys. Fluids B **3**, 3092 (1991).
[33]R. Kingham and A. Bell, J. Comput. Phys. **194**, 1 (2004).
[34]B. Chang, M. Marinak, C. Weber, and L. Peterson, 58th Annual Meeting of the American Physical Society Division of Plasma Physics (2016).
[35]B. Chang, J. Comput. Phys. **222**, 71 (2007).
[36]S.-M. Weng, Z.-M. Sheng, and J. Zhang, Phys. Rev. E **80**, 056406 (2009).
[37]R. P. Drake, Phys. Today, edited by L. Davison and Y. Horie, Graduate Texts in Physics, Vol. 63 (Cham, 2018) pp. 8–9.
[38]S. X. Hu, V. A. Smalyuk, V. N. Goncharov, S. Skupsky, T. C. Sangster, D. D. Meyerhofer, and D. Shvarts, Phys. Rev. Lett. **101**, 055002 (2008).
[39]G. Fiocco and E. Thompson, Phys. Rev. Lett. **10**, 89 (1963).
[40]R. F. Schmalz, Phys. Fluids **29**, 1389 (1986).
[41]J. Sanz, R. Betti, V. A. Smalyuk, M. Olazabal-Loume, V. Drean, V. Tikhonchuk, X. Ribeyre, and J. Feugeas, Phys. Plasmas **16**, 082704 (2009).